Journal of Environmental Chemical Engineering 9 (2021) 106287

Contents lists available at ScienceDirect

Journal of Environmental Chemical Engineering

journal homepage: www.elsevier.com/locate/jece

Calcium oxalate/calcium silicate hydrate (Ca-Ox/C-S-H) from blast furnace slag for the highly efficient removal of Pb^{2+} and Cd^{2+} from water

Quynh T.N. Le, Eleazer L. Vivas, Kuk Cho *

Department of Environmental Engineering, Pusan National University, 2, Busandaehak-ro 63beon-gil, Geumjeong-gu, Busan 46241, Republic of Korea

ARTICLE INFO

Editor: Dr. GL Dotto

Keywords:
Lead
Cadmium
Sorption
Ion exchange
Calcium oxalate
Calcium silicate hydrate

ABSTRACT

Heavy metal pollution of water is a global environmental concern which necessitates viable remediation through the exploration of highly effective adsorbents. Based on the affinity between oxalate and heavy metal, we synthesized a novel calcium oxalate/calcium silicate hydrate (Ca-Ox/C-S-H) adsorbent from blast furnace slag (BFS) by a facile oxalic acid/NaOH treatment. The BFS-derived Ca-Ox/C-S-H exhibited superior maximum uptake capacities for Pb^{2+} (2117 mg g^{-1}) and Cd^{2+} (1083 mg g^{-1}). The removal mechanism involves ion exchange, and adsorption kinetics showed an equilibration time of 10 min for Pb^{2+} at a solid-to-liquid ratio of 1.0 g L^{-1}, in agreement with both the pseudo-first- and pseudo-second-order reaction kinetics models. The adsorption isotherms of Ca-Ox/C-S-H for both metal ions also fitted the Sips model well. Ca-Ox/C-S-H showed high selectivity toward Pb^{2+} among various heavy metals and coexisting ions in water, and demonstrated high retention of adsorption capacity after being recycled up to four times. These results support the use of BFS-derived Ca-Ox/C-S-H as an efficient and economical Pb^{2+} and Cd^{2+} adsorbent.

1. Introduction

The volumes of toxic contaminants, such as heavy metals (HMs), organics, and pharmaceuticals, disposed into surface waters and groundwaters tend to increase in correspondence with increases in industrial activities, leading to significant harm to human health and ecological systems [1]. Due to their rates of bioaccumulation and the difficulty of degrading them into non-hazardous species, HMs are considered to be one of the more serious environmental pollution problems [2]. Pb and Cd are extremely hazardous HMs, and exposure to them can lead to digestive, skeletal, and nervous system diseases, and kidney, liver, and lung cancers [2]. Hence, the World Health Organization (WHO) has set the safe levels for Pb (10 ppb) and Cd (3 ppb) in drinking water [3]; and there is a serious need to develop efficient remediation technologies for removing Pb^{2+} and Cd^{2+} from wastewater to minimize their impact on human and environmental health.

To date, various technologies, including precipitation, electrodialysis, solvent extraction, and flocculation, have been employed to treat HM-contaminated water [4]. Although these techniques have shown high HM removal efficiencies in wastewater, they are accompanied by several disadvantages, such as excess sludge production, high cost, and complex operational requirements [4]. An alternative HM removal technique which is efficient, economical, and facile is adsorption. Thus, different adsorbent materials, such as clays, chalcogenides [5], layered double hydroxides (LDHs) [6], metal oxides [7], and metal organic frameworks (MOFs) [8] have recently been developed and applied for the sequestration of hazardous metals from water. However, many of these adsorbents have poor adsorption performance, require complicated preparation syntheses, and/or could generate secondary waste, thus hampering their practical application. To overcome these problems, industrial solid wastes-derived adsorbent materials have been utilized. Examples of waste materials used in developing efficient and cost-effective Pb^{2+} and Cd^{2+} adsorbents are corn straw biochar [9], coal fly ash (CFA) [10], and steel slag [11].

In pursuit of such promising adsorbents, calcium silicate hydrate (C-S-H), which is usually generated from the reaction of water and Portland cement [12], has drawn attention for its potential to remove toxic HMs, including Cu^{2+}, Cd^{2+}, Pb^{2+}, As^{5+}, Zn^{2+}, and Ni^{2+}, from water [11, 13–17]. C-S-H usually exhibits a decent adsorption capacity, owing to abundant concentrations of hydrated Ca^{2+} ions and hydroxyl groups, which partake in ion exchange and surface complexation with HMs, respectively [14]. Moreover, C-S-H can be synthesized from industrial solid wastes like steel slag and CFA, and demonstrates an adsorption capacity up to 508 mg g^{-1} for Pb^{2+} from industrial wastewater [11,18].

* Corresponding author.
E-mail address: kukcho@pusan.ac.kr (K. Cho).

https://doi.org/10.1016/j.jece.2021.106287
Received 7 July 2021; Received in revised form 24 August 2021; Accepted 25 August 2021
Available online 26 August 2021

Its adsorption capacity, however, must be further improved to enhance its removal performance for HMs.

Oxalate ($C_2O_4^{2-}$) has been utilized to recover metal ions, such as Pb^{2+}, Cd^{2+}, and Co^{2+}, from metal precipitates with oxalate ligands in industrial wastewater treatments [19]. Such metal ions have also been immobilized using oxalate-containing minerals like the naturally occurring Ca-Ox [20,21]. Ca-Ox synthesized from BFS was used as a Co^{2+} adsorbent, possessing the highest adsorption capacity ever reported [22]. Nonetheless, to the best of our knowledge, few researchers have explored the potential application of Ca-Ox for HM ions removal from water. We postulated that Ca-Ox derived from BFS can further enhance the capacity of slag-derived C-S-H for Pb^{2+} and Cd^{2+} uptake via an ion exchange mechanism.

Herein, an economical Ca-Ox/C-S-H adsorbent was prepared from BFS for Pb^{2+} and Cd^{2+} uptake from water. The Pb^{2+} and Cd^{2+} adsorption performances were evaluated in terms of uptake capacity, removal efficiency, and selectivity (i.e., distribution coefficient) at varying solution pH, contact time, initial concentrations, and in the existence of competitive cations. The recyclability of the Ca-Ox/C-S-H powder was also tested and the adsorption mechanism involved was determined.

2. Experimental

2.1. Ca-Ox/C-S-H preparation

The chemical composition of the BFS used to prepare Ca-Ox/C-S-H is presented in Table S1. All reagents were used as purchased without any purification.

40 mL of 0.75 mol L^{-1} $C_2H_2O_4$ (98%, Junsei Chemical Co., Ltd., Japan) and 10 mL of a 3 mol L^{-1} NaOH (97%, Daejung Chemicals and Metals Co., Ltd., South Korea) solution were added to 2.5 g of BFS and stirred vigorously at 293 K. The resulting solution was heated to 353 K and maintained at this temperature on a hot plate for 1 h. Subsequently, it was aged for 20 h at 353 K in a water bath to facilitate crystallization. Through centrifugation, the Ca-Ox/C-S-H product was collected and washed several times with deionized (DI) water until the pH of the supernatant was neutral. The rinsed product was vacuum-dried overnight at 383 K. Finally, it was pulverized using an agate mortar and pestle then stored in a clean glass vial.

2.2. Characterization

To identify the characteristic spectral peaks of the samples, Fourier transform infrared (FTIR) spectroscopy was conducted using IRAffinity-1 (Shimadzu, Japan). The spectra were obtained by accumulating scans in the range of 4000–500 cm^{-1}. The crystalline phases of the samples were identified using X-ray diffraction (XRD, X′pert^3 Powder, Malvern Panalytical Ltd., UK) with a Cu Kα radiation source (λ = 0.154 nm) at a generator voltage of 40 kV and tube current of 40 mA. The adsorption–desorption of N_2 was measured using a Micromeritics ASAP 2020 (USA) at 77 K, to determine the specific surface area (SSA) and pore volume of the materials. All samples were degassed at 150 °C under vacuum before SSA and porosity analysis. The elemental composition and distribution in and surface morphology of the adsorbent materials were determined using a scanning electron microscope (SEM, JCM-7000 NeoScope, JEOL Ltd., USA) with a built-in SEM energy dispersive X-ray spectrometer (SEM-EDS).

2.3. Batch adsorption experiments

The batch Pb^{2+} and Cd^{2+} adsorption experiments were conducted in triplicate at 298 K. Aqueous Pb^{2+} and Cd^{2+} solutions were prepared from $Pb(NO_3)_2.6H_2O$ (99%, Sigma Aldrich, USA) and $Cd(NO_3)_2.4H_2O$ (98%, Sigma Aldrich, USA). Adsorption performance at different solid-to-liquid ratios (S/L = 0.1–1.0 g L^{-1}) and solution pH values (3–7) was examined to determine optimum conditions for maximum HMs uptake. The solution pH was adjusted using small amounts of 0.01–1 mol L^{-1} NaOH or HCl (35–37 wt%, Samchun Pure Chemical Co., Ltd., South Korea) solutions. Adsorption isotherm experiments were conducted at various metal concentrations by diluting 1000 mg L^{-1} stock Pb^{2+} and Cd^{2+} solutions to determine the maximum adsorption capacity at an S/L = 0.1 g L^{-1}. The aqueous HM solutions were prepared at pH values 5.0 (Pb^{2+}) and 7.0 (Cd^{2+}) to ensure nil metal hydroxide precipitation within the concentration range of 10–1000 mg L^{-1}. After 10-h agitated (200 rpm) soaking of the adsorbent powder in an aqueous solution, the supernatant was filtered through a 0.22 μm membrane. The metal ion concentrations were measured using an atomic absorption spectrometer (AAS-200, PerkinElmer, Inc., USA) and inductively coupled plasma optical emission spectrometry (ICP-OES, PerkinElmer, USA). In the uptake kinetics studies, 2.5 or 25 mg of the adsorbent was soaked in 25 mL of 100 mg L^{-1} HM aqueous solution (Pb^{2+} or Cd^{2+}) at various contact times (t = 5 min to 15 h).

To determine the effects of co-existing ions on the Pb^{2+} and Cd^{2+} adsorption performances, five HM solutions of Pb^{2+}, Cd^{2+}, Zn^{2+}, Cu^{2+}, and Ni^{2+} were prepared with identical concentrations of 0.048 mmol L^{-1}. The following inorganic salts, which were supplied by Daejung Chemicals and Metals Co., Ltd. (South Korea), were used to prepare the other aqueous HM solutions: $NiCl_2$ (98%), $Zn(NO_3)_2.6H_2O$ (99%), and $CuCl_2.2H_2O$ (97.5%). Adsorption performance was also tested in artificial seawater (ASW, Coralife, USA), with the composition listed in Table S2. The Pb^{2+} and Cd^{2+} uptake performances of Ca-Ox/C-S-H were evaluated by calculating the adsorption capacity (Q_e, mg g^{-1}), removal efficiency (R, %), and distribution coefficient (K_d, mL g^{-1}) using Eqs. (1), (2), and (3), respectively.

$$Q_e = \frac{(C_o - C_e)V}{m} \quad (1)$$

$$R = \frac{(C_o - C_e)}{C_o} \times 100 \quad (2)$$

$$K_d = \frac{V}{m}\frac{C_o - C_e}{C_e} \quad (3)$$

Here, C_o (mg L^{-1}) and C_e (mg L^{-1}) represent the initial and equilibrium concentrations of metal ions, respectively; V (L) is the volume of the solution; and m (g) is the mass of the adsorbent.

For the recyclability test, 1.5 g of Ca-Ox/C-S-H was added to 1.5 L of Pb/Cd solution (C_o = 100 mg L^{-1}). The Pb/Cd-loaded adsorbents were collected after the adsorption experiment and washed with DI water three times to remove surface metal ions. Subsequently, at S/L = 1.0 g L^{-1}, the recovered solid residues were soaked in a glass bottle containing 1.5 L of 1.0 M $CaCl_2$ (Daejung Chemicals and Metals Co., Ltd., South Korea) solution and stirred for 15 h. The regenerated adsorbent was washed several times with DI water by vacuum filtration before being vacuum-dried at 60 °C for 12 h. Finally, adsorption tests were performed again. The above procedures were repeated up to four times.

3. Results and discussion

3.1. Adsorbent characteristics

Fig. 1a depicts the FTIR spectra of the pristine BFS and Ca-Ox/C-S-H from the chemically treated BFS samples. The BFS had the following characteristic spectral peaks: (1) metal oxides like Al_2O_3, CaO, and MgO (600–450 cm^{-1}); (2) O–H bond stretching (~3542 cm^{-1}); and (3) the Si–O (918 cm^{-1}) and Al–O (953 cm^{-1}) bonds [22]. The FTIR spectrum of the chemically treated BFS had the characteristic peaks for Ca-Ox and C-S-H [23–25], confirming the successful synthesis of Ca-Ox/C-S-H composite adsorbent. It had these characteristic spectral peaks: (1) the stretching vibrations of the –OH group from waters of crystallization (3448 and 1667 cm^{-1}); (2) the symmetric (1313 cm^{-1}) and asymmetric

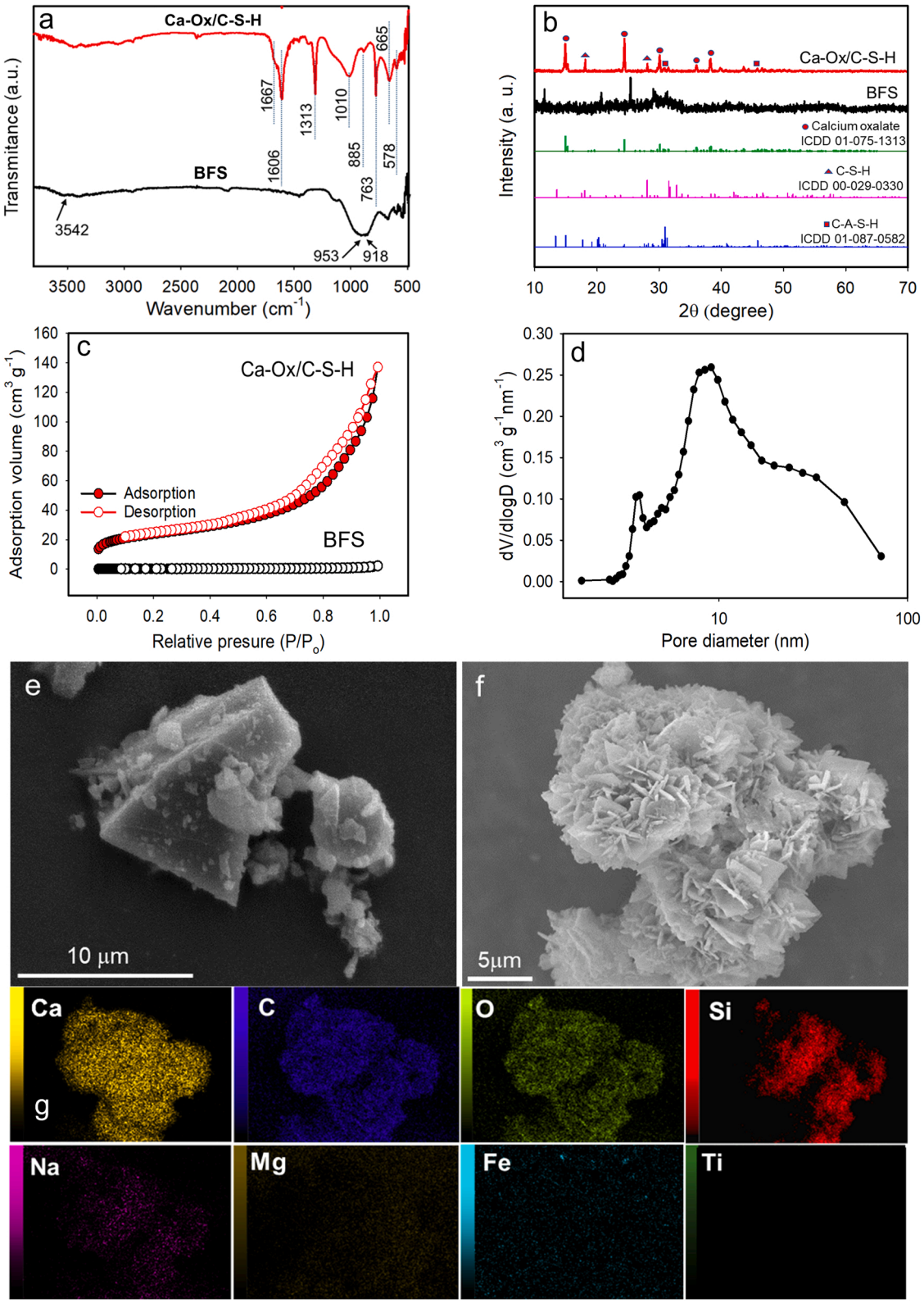

Fig. 1. (a) FTIR spectra, (b) diffractogram, (c) adsorption–desorption isotherms of N_2, (d) pore size distribution, SEM images of (e) raw and (f) chemically modified BFS, and (g) SEM-EDS maps of Ca-Ox/C-S-H composite adsorbent.

(1606 cm^{-1}) carboxyl group (–COO) stretching vibrations in Ca-Ox; (3) the asymmetric Si–O stretching vibration (1010 cm^{-1}), indicating the presence of C-S-H; (4) the plane bending of the O–C–O or Si–O Si groups (665 cm^{-1}); and (5) the stretching vibration of the C–C bond (763 and 885 cm^{-1}).

Fig. 1b shows the raw BFS and Ca-Ox or C-S-H XRD patterns. Gehlenite ($Ca_2Al[AlSiO_7]$), merwinite ($Ca_3Mg[SiO_4]_2$), and akermanite ($Ca_2Mg[Si_2O_7]$) are the primary crystalline phases found in the BFS [26]. Oxalate treatment of the BFS produced highly crystalline Ca-Ox/C-S-H, as high intensity Bragg peaks with flat backgrounds were

observed. The characteristic Bragg peaks corresponding to the Ca-Ox (whewellite) (ICDD 01 075 1313) were detected at 14.81° (001), 24.30° (020), and 30.18° (002). Meanwhile, the peaks located at 17.50° (112) and 28.09° (310) were ascribed to the C-S-H crystals (ICDD 00 029 0330). Furthermore, the low-intensity peaks observed at 30.94° (351) and 45.86° (191) verified some presence of calcium aluminum silicate hydrate (C-A-S-H) crystals (ICCD 01 087 0582), suggesting that aluminum and silicon participated in the formation of the C-S-H matrix [27]. These crystallographic identifications are also corroborated by elemental analysis. Ca-Ox crystals grew from the reaction of the inherent Ca in the BFS and the $C_2O_4^{2-}$ ligand after the addition of oxalic acid. Simultaneously, C-S-H crystals were produced through the reaction between NaOH solution and Ca and Si which are both inherently present in the BFS [11]. The oxalated BFS without alkalinization did not exhibit peaks corresponding to the C-S-H crystal (Fig. S1). The C-S-H crystals were not observed when BFS was alkalinized because Ca-Ox had nucleated before the addition of an alkaline activator [22]. Calcium ions completely reacted with $C_2O_4^{2-}$, inhibiting the formation of C-S-H. The simultaneous addition of $H_2C_2O_4$ and alkaline solutions resulted in the correspondingly simultaneous formation of Ca-Ox and C-S-H.

The adsorption–desorption isotherms of N_2 for the raw and modified BFS samples are depicted in Fig. 1c and summarized in Table S3. The pristine BFS had a low SSA of 0.96 $m^2\ g^{-1}$. A type IV isotherm was observed for Ca-Ox/C-S-H, indicating that it is a mesoporous material [28]. The mesoporosity of the composite is supported by the Barrett–Joyner–Halenda pore size distribution as depicted in Fig. 1d. Improvement in the SSA (82.2 $m^2\ g^{-1}$) and pore volume (0.21 $cm^3\ g^{-1}$) was observed for Ca-Ox/C-S-H. Increase in the SSA can be attributed to the Ca-Ox and C-S-H crystallization from the reaction of BFS powder with $C_2H_2O_4$ and NaOH solutions [11,23].

The raw BFS particles were irregularly shaped with relatively smooth surfaces as observed in the images (Fig. 1e) captured through SEM images. Ca-Ox/C-S-H contained plenty of hexagonal plate aggregates (Fig. 1f). The elemental maps (Fig. 1g) show uniform distribution of Ca, O, and C, and Si-rich zones, which were probable C-S-H sites, as supported by the diffraction patterns (Fig. 1b) obtained through XRD. The elemental mapping images of Ca-Ox/C-S-H samples revealed the absence of Mg, Fe, and Ti. Minor quantities of Na were observed in the same locations as Si, implying that Na^+ ions cooperated in C-S-H synthesis. Table S4 shows the chemical composition of Ca-Ox/C-S-H which was qualitatively determined through SEM-EDS. The Ca content in Ca-Ox was up to 88% of the total Ca in Ca-Ox/C-S-H, implying that Ca-Ox contributed a key function in the Pb^{2+} and Cd^{2+} removal.

3.2. Adsorption

3.2.1. Influence of initial pH and adsorbent dose

Fig. 2a depicts the effect of initial solution pH on the Pb^{2+} and Cd^{2+} removal performance of Ca-Ox/C-S-H. Increasing removal efficiency (R) was observed for Pb^{2+} (89–99.8%) and Cd^{2+} (62–91%) at increasing pH values (3.0–7.0). Additionally, the distribution coefficients (K_d) for Pb^{2+} (K_d^{Pb}) and Cd^{2+} (K_d^{Cd}) increased (K_d^{Pb} $= 6.1 \times 10^3$ to 5.6×10^5 mL g^{-1}, $K_d^{Cd} = 1.6 \times 10^3$ to 1.2×10^4 mL g^{-1}) as solution pH increased. Typically, materials with a K_d value greater than 10^4 mL g^{-1} are regarded as exceptional adsorbents for the selective removal of contaminants [29]. Table S5 summarizes the uptake selectivities of different adsorbents. Ca-Ox/C-S-H demonstrated higher K_d values than those of other low-cost material- or waste-derived adsorbents like biochar-$MnFe_2O_4$ ($K_d^{Cd} = 1.3 \times 10^3$ mLg^{-1}) [9], chitosan-C-S-H ($K_d^{Pb} = 2.9 \times 10^5$ mLg^{-1}) [30], HAP/C-S-H ($K_d^{Pb} = 3.5 \times 10^4$ mLg^{-1}) [13], C-S-H from steel slag ($K_d^{Pb} = 6.0 \times 10^4$ mLg^{-1}) [11], and HM-CFB-FA from CFA ($K_d^{Cd} = 4.1 \times 10^3$ mLg^{-1}) [10].

Fig. S2 shows that the Ca-Ox/C-S-H had negative zeta potential values at pH 3 and steadily decreased as pH increased. This can explain the increase in R and K_d with increasing pH because of the increased

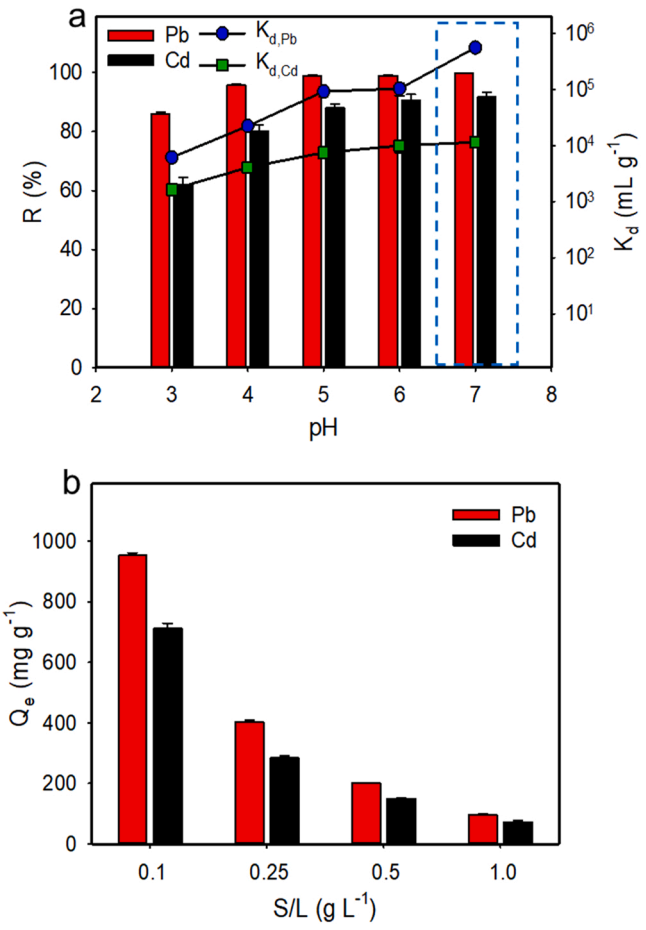

Fig. 2. (a) Removal efficiency (R) and K_d values at different pH levels at C_o = 10 mg L^{-1} and S/L = 1.0 g L^{-1}; and (b) influence of S/L on HM uptake capacity (C_o = 100 mg L^{-1}, pH_{Pb} = 5, pH_{Cd} = 7). General adsorption conditions: t = 15 h, T = 298 K.

electrostatic attraction between the more negative surfaces of Ca-Ox/C-S-H and Pb^{2+} and Cd^{2+} ions. To determine if precipitation contributed to the high R values, the species distributions of Pb^{2+} and Cd^{2+} at varying solution pH values were evaluated (Fig. S3). At acidic conditions (i.e., pH range of 2–6), the dominant species was Pb^{2+} which started to precipitate as lead hydroxide at approximately above pH 8, an observation consistent with previous studies [9,13]. Cd^{2+} was dominant in the pH range of 2–8. Thus, precipitation at the pH range investigated in the present study is unlikely to occur. The drop in Pb^{2+} and Cd^{2+} R values at pH 3 could be attributed to the competing H^+ ions which inhibited metal adsorption. Under acidic conditions, the instability of C-S-H in Ca-Ox/C-S-H do not contribute to the reduction in metal uptake because Ca-Ox/C-S-H retained its crystal stability (Fig. S4). Considering the above results, further Pb^{2+} (pH = 5) and Cd^{2+} (pH = 7) adsorption experiments were conducted.

The optimum S/L values for the maximum Pb^{2+} and Cd^{2+} adsorption capacities were determined. Fig. 2b depicts that the Pb^{2+} adsorption capacity declined from 994.02 to 98.14 mg g^{-1} as the S/L increased from 0.1 to 1.0 g L^{-1}. Cd^{2+} uptake also demonstrated a descending trend, decreasing from 711.05 to 66.64 mg g^{-1}. The removal efficiency of Pb^{2+} at all S/L values was 97.5%. The highest capacity obtained at 0.1 g L^{-1} was attributed to relatively more available Pb^{2+}.

3.2.2. Adsorption kinetics

The uptake kinetics with Ca-Ox/C-S-H were examined at S/L values of 0.1 and 1.0 g L^{-1}. The adsorption capacity for a given time interval (Q_t) increased while residual metal concentrations rapidly decreased

with time as depicted in Fig. 3. At S/L = 1.0 g L^{-1}, the Pb^{2+} and Cd^{2+} Q_t values both sharply increased within the first 5 min, reaching equilibrium thereafter. Equilibrium was reached at faster rates at higher than at lower S/L values. For Pb^{2+}, the equilibration times at the S/L values of 1.0 and 0.1 g L^{-1} were approximately 10 and 60 min, respectively. For Cd^{2+}, the equilibration times at the S/L values of 1.0 and 0.1 g L^{-1} were approximately 60 and 120 min, respectively.

Nonlinear regressions of the uptake kinetics data were performed using the conventional reaction kinetics models, namely pseudo-first-order (PFO) and pseudo-second-order (PSO) expressed by Eqs. (4) and (5), respectively [9].

$$Q_t = Q_e(1 - e^{-k_1 t}) \tag{4}$$

$$Q_t = \frac{k_2 Q_e^2 t}{1 + k_2 Q_e t} \tag{5}$$

Here, Q_t (mg g^{-1}) is the uptake capacity at time t (min); Q_e (mg g^{-1}) is the equilibrium adsorption capacity; and k_1 (min^{-1}) and k_2 (g mg^{-1} min^{-1}) are the PFO and PSO rate constants, respectively.

Table 1 summarizes the adsorption kinetics constants. The experimental kinetics data well fitted the two reaction kinetics models, with the calculated equilibrium adsorption values being comparable to the experimental data. The k_2 values significantly improved for Pb^{2+} ($\sim 10^{-4}$ to $\sim 10^{-3}$ g mg^{-1} min^{-1}) and Cd^{2+} ($\sim 10^{-4}$ to $\sim 10^{-2}$ g mg^{-1} min^{-1}) by increasing the S/L. More adsorption sites at higher S/L values resulted in quicker Pb^{2+} and Cd^{2+} removal.

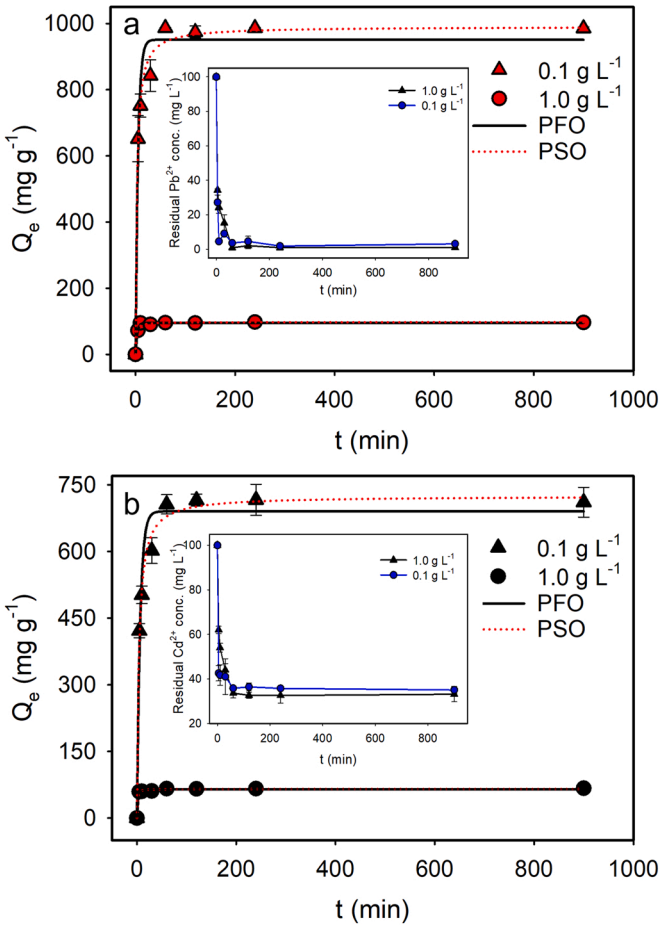

Fig. 3. Adsorption kinetics at C_o = 100 mg $L^{-1}$and S/L = 0. 1 and 1.0 g L^{-1} using Ca-Ox/C-S-H composite material (Q_t vs. t): nonlinear regressions of PFO and PSO models for (a) Pb^{2+} (pH_{Pb} = 5) and (b) Cd^{2+} (pH_{Cd} = 7) with insets of residual HM concentration-time profiles. General adsorption conditions: t = 15 h, T = 298 K.

For further investigation of the adsorption behavior, the intraparticle diffusion model was used in evaluating the uptake kinetics data. Fig. S5 shows that the multilinear portions of the Q_t versus $t^{0.5}$ plots for Pb^{2+} and Cd^{2+} do not pass through the origin, suggesting that Pb^{2+} and Cd^{2+} uptake by Ca-Ox/C-S-H was not controlled by intraparticle diffusion alone, but was a multistep process [31]. The first stage was due to external surface adsorption, in which the uptake rates of Pb^{2+} and Cd^{2+} were high due to the large concentration difference between Pb^{2+} and Cd^{2+} in solution and at the surfaces of Ca-Ox/C-S-H. The second, mostly linear stage indicates slow intraparticle pore diffusion, leading to slow adsorption rates over prolonged contact times.

3.2.3. Adsorption isotherms

Adsorption experiments at initial metal concentrations of 10–1000 mg L^{-1} at 298 K were carried out to determine the maximum Pb^{2+} and Cd^{2+} uptake capacities of Ca-Ox/C-S-H. Fig. 4a depicts the dramatic improvement of capacities for adsorbing Pb^{2+} (81.7–2018 mg g^{-1}) and Cd^{2+} (62.5–1059 mg g^{-1}) as initial concentration increased. The metal uptake capacity increased as the initial concentration increased, a behavior that can be ascribed to the greater availability of HM ions in an aqueous solution. Additionally, higher initial concentration provided a larger driving force to overpower the different resistances of the HM ions in the solution with respect to mass transfer between solid phases. This was likely due to the higher frequency of collisions between Pb^{2+} and Cd^{2+} ions and the adsorbent active sites, resulting in greater adsorption capacities [1]. However, the adsorption capacities did not further increase, indicating that saturation was achieved due to the full occupancy of adsorption sites.

Nonlinear fittings of the adsorption isotherm data into the Langmuir, Freundlich, and Sips models expressed by Eqs. (6), (7), and (8), respectively were done to determine the adsorption behavior of Ca-Ox/C-S-H for Pb^{2+} and Cd^{2+}.

$$Q_e = \frac{Q_m K_L C_e}{1 + K_L C_e} \tag{6}$$

$$Q_e = K_F C_e^{\frac{1}{n_F}} \tag{7}$$

$$Q_e = \frac{Q_m K_S C_e{}^{n_S}}{1 + K_S C_e{}^{n_S}} \tag{8}$$

where Q_m (mg g^{-1}) is the hypothetical maximum Pb^{2+} or Cd^{2+} Q_e value; K_L (L mg^{-1}) is the Langmuir constant representing the uptake rate; K_S ((L mg^{-1})^n) is the Sips equilibrium constant in relation to the energy of adsorption; K_F (mg g^{-1} (L mg^{-1})$^{1/n}$) and dimensionless n_F are the Freundlich empirical constants; and n_S is the dimensionless Sips constant which denotes the heterogeneity of the adsorption sites [8]. Table 2 lists the parameters of the adsorption models.

Fig. 4a depicts that the Pb^{2+} and Cd^{2+} adsorption isotherms for Ca-Ox/C-S-H best fits the Sips isotherm model as corroborated by the high correlation coefficient (r^2) values for Pb^{2+} (r^2 = 0.9876) and Cd^{2+} (r^2 = 0.9972). At high surface coverage, the Sips and Langmuir isotherms share similar characteristics [32], and at low surface coverage, the adsorption behavior approaches to the Freundlich isotherm [33]. Furthermore, the n_S values for Pb^{2+} (n_S = 0.5888) and Cd^{2+} (n_S = 0.7211) were not close to unity, implying that Ca-Ox/C-S-H has heterogeneous sorption sites [33]. The calculated Sips Q_m values for Cd^{2+} and Pb^{2+} were 1083 and 2117 mg g^{-1}, respectively. These values were similar to the theoretical capacities for adsorbing Cd^{2+} (1300 mg g^{-1}) and Pb^{2+} (2392 mg g^{-1}) as per the calculations made using the EDS results.

Comparisons of the adsorption performance of Ca-Ox/C-S-H and various adsorbent materials toward Pb^{2+} and Cd^{2+} are depicted in Fig. 4b and summarized in Table S5. At present, Ca-Ox/C-S-H demonstrates the highest Q_m compared with other more complicated

Table 1
Uptake kinetics constants of Pb^{2+} and Cd^{2+} on Ca-Ox/C-S-H.

	S/L (g L^{-1})	$Q_{e,exp}$ (mg g^{-1})	PFO			PSO		
			k_1 (min^{-1})	$Q_{e,cal}$ (mg g^{-1})	r^2	k_2 (g mg^{-1} min^{-1})	$Q_{e,cal}$ (mg g^{-1})	r^2
Pb^{2+}	0.1	985.7 ± 4.01	0.1977	950.53	0.9710	3.5×10^{-4}	990.46	0.9919
	1.0	96.54 ± 1.07	0.2999	95.73	0.9933	7.8×10^{-3}	97.64	0.9856
Cd^{2+}	0.1	771.1 ± 33.6	0.1554	690.31	0.9702	3.4×10^{-4}	724.60	0.9929
	1.0	66.91 ± 1.60	0.4819	64.52	0.9889	2.3×10^{-2}	65.66	0.9948

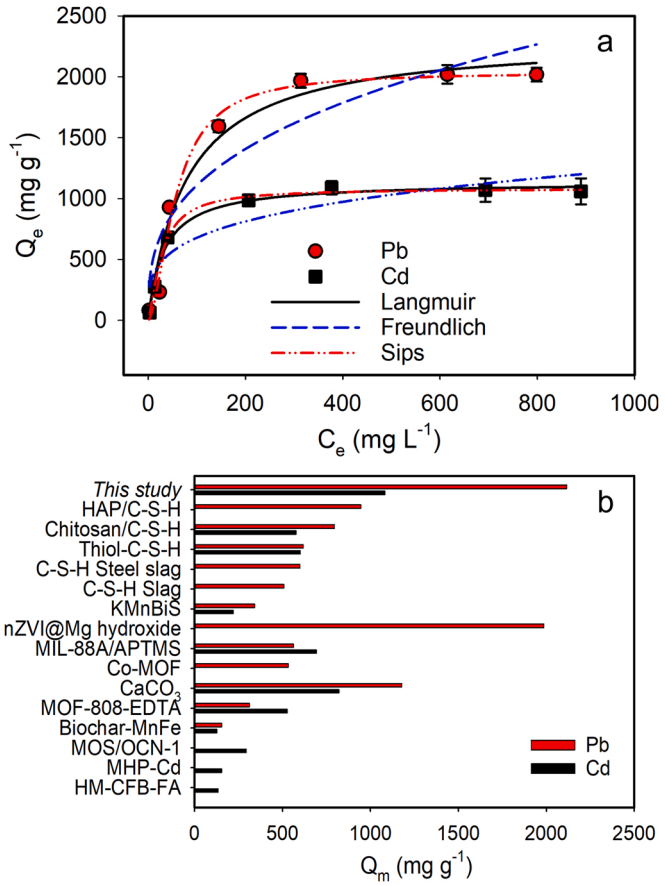

Fig. 4. Equilibrium HM adsorption performance of Ca-Ox/C-S-H: (a) Q_e vs. C_e plots for Pb^{2+} and Cd^{2+} with nonlinear fittings of the adsorption models (adsorption conditions: C_o = 10–1000 mg L^{-1}, S/L = 0.1 g L^{-1}, pH_{Pb} = 5, pH_{Cd} = 7, t = 10 h, T = 298 K); (b) comparisons of Q_m^{Pb} and Q_m^{Cd} of various adsorbents.

adsorbents, including MOF, and inorganic materials like $K_x[Bi_{4-x}Mn_xS_6]$ (342.4 mg Pb^{2+} g^{-1}, 21.2 mg Cd^{2+} g^{-1}) [5], MIL-88A(Fe)/APTMS (563.2 mg Pb^{2+} g^{-1}, 693 mg Cd^{2+} g^{-1}) [34], MOF-808-EDTA (313 mg Pb^{2+} g^{-1}) [35], MOS/OCN-1 (293.8 mg Cd^{2+} g^{-1}) [36], magnetic calcium carbonate adsorbents (MCCR-350, 1179.1 mg Pb^{2+} g^{-1}, 821.4 mg Cd^{2+} g^{-1}) [31], and nZVI@$Mg(OH)_2$ (1986.6 mg Pb^{2+} g^{-1}) [7]. The Q_m of Ca-Ox/C-S-H was also higher than that of low-cost material- or waste-derived adsorbents, such as C-S-H from slag (508 mg Pb^{2+} g^{-1}) [11], fluidized bed fly ash (CFB-FA, 134.9 mg Cd^{2+} g^{-1}) [10], chitosan-coated C-S-H (796 mg Pb^{2+} g^{-1}, 578 mg Cd^{2+} g^{-1}) [30], HAP/C-S-H (946.7 mg Pb^{2+} g^{-1}) [13], and thiol-C-S-H (618.09 mg Pb^{2+} g^{-1}, 601.51 mg Pb^{2+} g^{-1}) [37]. The superior adsorption performance of Ca-Ox/C-S-H can be attributed to its abundant $C_2O_4^{2-}$ and SiO^- sites for ion exchange and to the attraction of cationic metals to the surfaces on the adsorbent substrate that have negative charges.

Table 2
Adsorption isotherm constants for Pb^{2+} and Cd^{2+} on Ca-Ox/C-S-H.

Model and parameter	Value	
	Pb^{2+}	Cd^{2+}
Langmuir		
Q_m (mg g^{-1})	2332	1136
K_L (L mg^{-1})	0.0125	0.0308
r^2	0.9693	0.9896
Freundlich		
K_F (mg g^{-1} (L $mg^{-1})^{1/n}$)	227.82	202.80
n_F	0.0338	0.2619
r^2	0.8777	0.8599
Sips		
Q_m (mg g^{-1})	2117	1083
K_s ((L $mg^{-1})^n$)	0.0010	0.0098
n_S	0.5888	0.7211
r^2	0.9876	0.9972

3.2.4. *Influence of competing ions and investigation of regeneration*

Commonly, several other HM ions, including Cu^{2+}, Ni^{2+}, and Zn^{2+}, coexist with Cd^{2+} and Pb^{2+}in wastewater. This coexistence of various HM ions could depreciate the uptake capability of Ca-Ox/C-S-H. Thus, the effect of the co-existence of the aforementioned ions at constant molar concentrations on the Pb^{2+} and Cd^{2+} adsorption selectivities of Ca-Ox/C-S-H was investigated with the R values depicted in Fig. 5a. For Pb^{2+}, Ca-Ox/C-S-H exhibited an R value of 98.8% and a K_d value of 8.0×10^4 mL g^{-1}, indicating its high Pb^{2+} uptake selectivity. On the other hand, the values of R and K_d for Cd^{2+} declined to 62% and 1.6×10^3 mL g^{-1}, respectively compared with the results of single cation (Cd^{2+}) adsorption experiments. The selectivity for other ions was in the order of Cu^{2+} (R = 33.2%), Ni^{2+} (R = 28.7%), and Zn^{2+} (R = 26.2%). K_d followed the same trend as that for R (Table S6). The separation factor (SF), another measure of adsorption selectivity, for two metal ions ($SF_{A/B}$) were computed from K_d^A / K_d^B [1]. Ca-Ox/C-S-H indeed had higher Pb^{2+} uptake selectivity, as its SF values for Pb^{2+} over co-existing HM ions are greater than 100 [38]; specifically, $SF_{Pb/Zn}$ = 222, $SF_{Pb/Cu}$ = 159, and $SF_{Pb/Ni}$ = 200. This can be explained by two factors. First, the similar ionic radii of Pb^{2+} (1.19 Å) and Ca^{2+} (1.00 Å) allows the former to be exchanged relatively easily with the latter in the Ca-Ox/C-S-H structure. On the other hand, considerably smaller HM ions like Ni^{2+} (0.69 Å), Cu^{2+} (0.73 Å), and Zn^{2+} (0.75 Å) possess lesser affinity for the crystal lattice of the Ca-Ox/C-S-H composite, resulting in inferior R values for such ions [39]. Second, the hydration enthalpy changes for ion exchange were negative (more stable) for Pb^{2+}/Ca^{2+} and positive (less stable) for Cd^{2+}/Ca^{2+} [40]. The hydration enthalpies of Ca^{2+}, Pb^{2+}, and Cd^{2+} were −1577, −1481, and −1807 kJ/mol, respectively [41]. This was the reason for the low selectivity of Ca-Ox/C-S-H for Cd^{2+}, even though its ionic radius (0.95 Å) is similar to that of Ca^{2+}. Additionally, the stability constant showed that Pb-Ox was more stable than Cd-Ox [42].

Major naturally occurring cations (e.g., K^+, Ca^{2+}, Na^+, Mg^{2+}) and

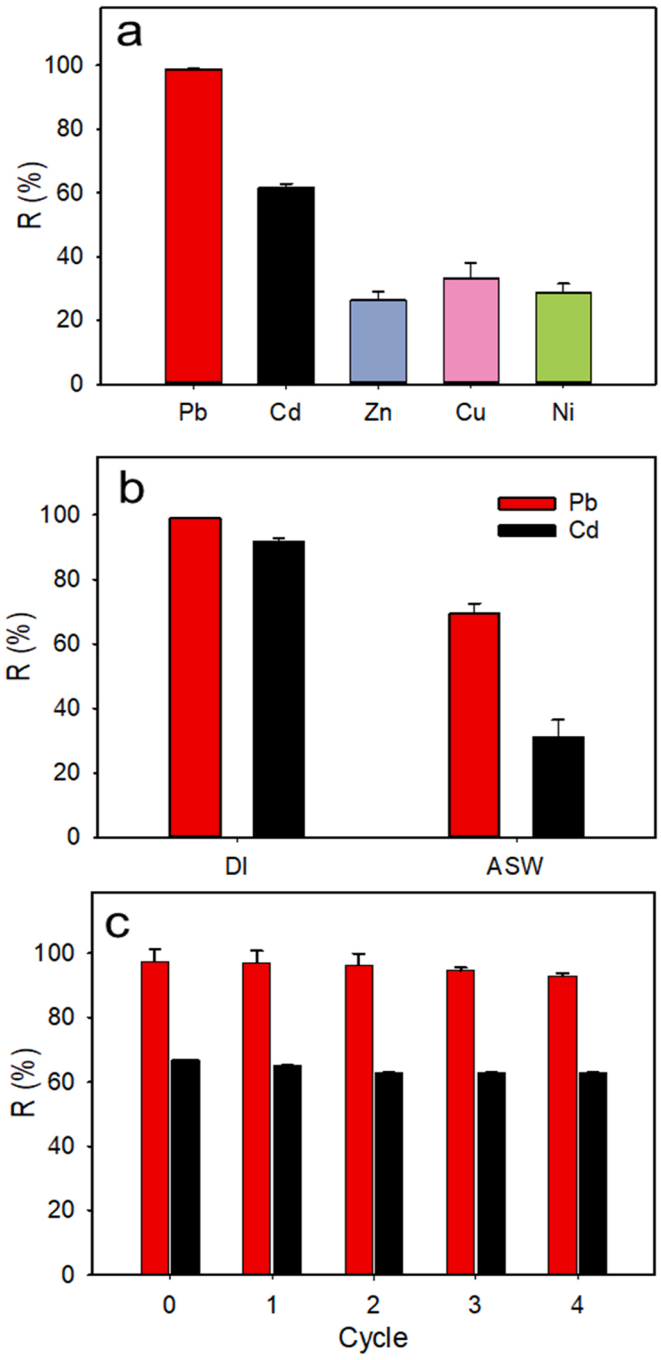

Fig. 5. Metal uptake selectivity of Ca-Ox/C-S-H: effect of competing (a) HM ion in aqueous solution and (b) cations in ASW; (c) recyclability of Ca-Ox/C-S-H. Adsorption conditions: HM C_o = 0.048 mmol L^{-1}, S/L = 1.0 g L^{-1}, pH = 5.0, t = 10 h.

anions (e.g., CO_3^{2-}, Cl^-, HCO_3^-, HPO_4^{2-}, SO_4^{2-}) present in bodies of water can hinder the adsorption of a target HM ion for they compete for the adsorbent active sites. The Pb^{2+} and Cd^{2+} removal efficiencies in ASW were measured. Even at an extremely saline condition, the Ca-Ox/C-S-H exhibited high Pb^{2+} R value of 70%, revealing the superior selectivity of Ca-Ox/C-S-H toward Pb^{2+} in ASW (Fig. 5b). As the concentration of competing ions is much lower in rivers [43], industrial wastewater [44], or mine water [45] than that in ASW, Ca-Ox/C-S-H can be a promising Pb^{2+} and Cd^{2+} adsorbent for the remediation of different types of water.

Fig. 5c shows the results of the conducted recyclability experiment for Ca-Ox/C-S-H. After four adsorption-desorption cycles, the regenerated composite adsorbent exhibited R values of 93% and 63% for Pb^{2+} and Cd^{2+}, respectively, highlighting the possible application of Ca-Ox/C-S-H as a reclaimable adsorbent for the remediation of waters contaminated by Pb^{2+} and/or Cd^{2+}. There was no significant change in the crystallinity of Ca-Ox/C-S-H after regeneration (Fig. S6).

3.2.5. Adsorption mechanism

Ion exchange mechanisms can expound how the Ca-Ox/C-S-H composite adsorbent sequesters Pb^{2+} and Cd^{2+} from aqueous solutions. The results of the inductively coupled plasma analysis of liquid samples for Ca^{2+}, Cd^{2+}, and Pb^{2+} are listed in Table S7. The Ca^{2+} concentration increased while Cd^{2+} and Pb^{2+} concentrations decreased after adsorption. The calculated molar ratios of released Ca^{2+} to adsorbed Cd^{2+} (0.904) and Pb^{2+} (0.929) were close to unity; thus, revealing that ion exchange was the dominant mechanism in the Cd^{2+} and Pb^{2+} removal from water. HM removal by Ca-Ox and C-S-H through ion exchange had been well elucidated in previous studies [11,21,22,46]. More metal ions were adsorbed than the amount of Ca^{2+} ions released, implying the possible complexation of the metal ions on the Ca-Ox/C-S-H surface.

Fig. S7 depicts the XRD patterns of the pristine adsorbent and the solid residue collected after adsorption. Evident differences between the diffraction patterns of pristine Ca-Ox/C-S-H and solid residues after adsorption were observed. The uptake of Pb^{2+} caused the characteristic Bragg peaks relating to the (020) and (001) planes of Ca-Ox/C-S-H to move to the left (i.e., lower 2θ values), indicating reduced d spacing which was likely because of the favorable smaller Ca^{2+}–larger Pb^{2+} ion exchange as expounded in terms of ionic radius in Section 3.2.5. In contrast, after Cd^{2+} adsorption, these peaks shifted to the right (i.e., higher 2θ values), likely because of the smaller ionic radius of Cd^{2+} (0.95 Å) than that of the parent cation Ca^{2+}. After Cd^{2+} and Pb^{2+} adsorption, crystalline peak characteristics which match the crystal phases of cadmium oxalate (ICDD 00 054 0317) and lead oxalate (ICDD 00 014 0803), respectively were observed. A small fraction of lead silicate (ICDD 00 032 0537) and cadmium silicate (ICDD 00 026 0272) might also have contributed to the peaks. At higher initial Pb^{2+} and Cd^{2+} concentrations, the decrease in Ca-Ox peaks and the appearance of metal crystal phases also corroborated the ion exchange between Pb^{2+} and Cd^{2+} and Ca^{2+}. Fig. S8 shows the FTIR spectra of the collected solid residues after adsorption. The characteristic spectral peaks for Si–O (1010 cm^{-1}) and O–C–O (665 cm^{-1}) bonds moved to 1023 and 655 cm^{-1}, respectively, implying the possibility of complexation between the carboxyl/hydroxyl groups and metal ions [1,9,37].

The morphologies of the as-prepared Ca-Ox/C-S-H and solid residues after adsorption experiments were alike, signifying that Ca-Ox/C-S-H was structurally and chemically stable (Fig. 1e and S9). Moreover, the elemental maps revealed that the amount of Ca^{2+} decreased while the amounts of Cd^{2+} and Pb^{2+} increased, and the latter ions were homogeneously distributed over the solid residue collected after adsorption. These qualitative results support the inference that ion exchange between Pb^{2+} and Cd^{2+} and Ca^{2+} is the major mechanism through which Ca-Ox/C-S-H adsorbs Pb^{2+} and Cd^{2+} ions from water.

4. Conclusions

Herein, a neoteric Ca-Ox/C-S-H composite adsorbent was synthesized from BFS for Pb^{2+} and Cd^{2+} removal. It demonstrated superior maximum capacities for adsorbing Pb^{2+} (2117 mg g^{-1}) and Cd^{2+} (1083 mg g^{-1}), which are among the highest adsorption capacities reported to date. The adsorption isotherm followed the Sips model, implying both Langmuir and Freundlich adsorption. The composite also exhibited rapid Pb^{2+} and Cd^{2+} adsorption, and the uptake kinetics data well fitted both the PFO and PSO reaction kinetics models. At pH = 3–7, stable HM removal performance was observed with ion exchange as the dominant adsorption mechanism involved. Furthermore, Ca-Ox/C-S-H demonstrated high Pb^{2+} uptake selectivities in aqueous solutions with other HMs and in ASW. Lastly, it was able to maintain its adsorption

performance after four adsorption-desorption cycles. In view of these findings, Ca-Ox/C-S-H is a promising Pb^{2+}/Cd^{2+} adsorbent for water remediation.

Funding

This work was supported by a 2-year research grant of Pusan National University, a National Research Foundation (NRF) grant, which is funded by the Ministry of Science and ICT, Republic of Korea (2019R1A2C1084995), and by the Basic Science Research Program through the NRF, which is funded by the Ministry of Education, Republic of Korea (2020R1A6A1A03044834).

CRediT authorship contribution statement

Quynh T. N. Le: Conceptualization, Methodology, Investigation, Writing – original draft. **Eleazer L. Vivas:** Writing – review & editing. **Kuk Cho:** Validation, Supervision, Writing – review & editing.

Declaration of Competing Interest

The authors declare that they have no known competing financial interests or personal relationships that could have appeared to influence the work reported in this paper.

Appendix A. Supporting information

Supplementary data associated with this article can be found in the online version at doi:10.1016/j.jece.2021.106287.

References

[1] C. Xiong, S. Wang, P. Hu, L. Huang, C. Xue, Z. Yang, X. Zhou, Y. Wang, H. Ji, Efficient selective removal of Pb (II) by using 6-aminothiouracil-modified Zr-based organic frameworks: from experiments to mechanisms, ACS Appl. Mater. Interfaces 12 (2020) 7162–7178.
[2] A. Khan, S. Khan, M.A. Khan, Z. Qamar, M. Waqas, The uptake and bioaccumulation of heavy metals by food plants, their effects on plants nutrients, and associated health risk: a review, Environ. Sci. Pollut. Res. 22 (2015) 13772–13799.
[3] WHO, Guidelines for drinking-water quality, in, 2017.
[4] A. Azimi, A. Azari, M. Rezakazemi, M. Ansarpour, Removal of heavy metals from industrial wastewaters: a review, ChemBioEng Rev. 4 (2017) 37–59.
[5] R. Wang, H. Chen, Y. Xiao, I. Hadar, K. Bu, X. Zhang, J. Pan, Y. Gu, Z. Guo, F. Huang, $K_x[Bi_{4-x}Mn_xS_6]$, design of a highly selective ion exchange material and direct gap 2D semiconductor, J. Am. Chem. Soc. 141 (2019) 16903–16914.
[6] F. Lyu, H. Yu, T. Hou, L. Yan, X. Zhang, B. Du, Efficient and fast removal of Pb^{2+} and Cd^{2+} from an aqueous solution using a chitosan/Mg-Al-layered double hydroxide nanocomposite, J. Colloid Interface Sci. 539 (2019) 184–193.
[7] M. Liu, Y. Wang, L. Chen, Y. Zhang, Z. Lin, $Mg(OH)_2$ supported nanoscale zero valent iron enhancing the removal of Pb(II) from aqueous solution, ACS Appl. Mater. Interfaces 7 (2015) 7961–7969.
[8] Q.T.N. Le, K. Cho, Caesium adsorption on a zeolitic imidazolate framework (ZIF-8) functionalized by ferrocyanide, J. Colloid Interface Sci. 581 (2021) 741–750.
[9] L. Zhang, J. Guo, X. Huang, W. Wang, P. Sun, Y. Li, J. Han, Functionalized biochar-supported magnetic $MnFe_2O_4$ nanocomposite for the removal of Pb(II) and Cd(II), RSC Adv. 9 (2019) 365–376, https://doi.org/10.1039/C8RA09061K.
[10] R. Qiu, F. Cheng, H. Huang, Removal of Cd^{2+} from aqueous solution using hydrothermally modified circulating fluidized bed fly ash resulting from coal gangue power plant, J. Clean. Prod. 172 (2018) 1918–1927.
[11] N. Shao, S. Tang, Z. Liu, L. Li, F. Yan, F. Liu, S. Li, Z. Zhang, Hierarchically structured calcium silicate hydrate-based nanocomposites derived from steel slag for highly efficient heavy metal removal from wastewater, ACS Sustain. Chem. Eng. 6 (2018) 14926–14935.
[12] I.G.J.C. Richardson, c. research, The calcium silicate hydrates, 38 (2008) 137–158.
[13] Z. Zhang, X. Wang, H. Wang, J. Zhao, Removal of Pb (II) from aqueous solution using hydroxyapatite/calcium silicate hydrate (HAP/CSH) composite adsorbent prepared by a phosphate recovery process, Chem. Eng. J. 344 (2018) 53–61.
[14] J. Li, J. Zhang, X. Wu, J. Zhao, M. Wu, W. Huan, A nanocomposite paper comprising calcium silicate hydrate nanosheets and cellulose nanofibers for high-performance water purification, RSC Adv. 10 (2020) 30304–30313, https://doi.org/10.1039/D0RA05513A.
[15] F. Valenzuela, G. Quintana, A. Briso, V. Ide, C. Basualto, J. Gaete, G.J.Jo.W.P.E. Montes, Cu(II), Cd(II), Pb(II) and As(V) adsorption from aqueous solutions using magnetic iron-modified calcium silicate hydrate: Adsorption kinetic analysis, 40 (2021) 101951.
[16] Y. Zhao, H. Chen, Q.J.E.T. Yan, Innovation, Enhanced phosphate removal during the simultaneous adsorption of phosphate and Ni2+ from electroless nickel wastewater by calcium silicate hydrate (CSH), 8 (2017) 141–149.
[17] N. Labhasetwar, O.J.Joms Shrivastava, Ca2+⇌ Pb2+ exchange reaction of calcium silicate hydrate: Ca5Si6O18 H2·4H2O, 24 (1989) 4359–4362.
[18] J. Ma, G. Qin, Y. Zhang, J. Sun, S. Wang, L. Jiang, Heavy metal removal from aqueous solutions by calcium silicate powder from waste coal fly-ash, J. Clean. Prod. 182 (2018) 776–782.
[19] A. Verma, R. Kore, D.R. Corbin, M.B. Shiflett, Metal recovery using oxalate chemistry: a technical review, Ind. Eng. Chem. Res. 58 (2019) 15381–15393.
[20] D.M. Singer, S.B. Johnson, J.G. Catalano, F. Farges, G.E. Brown Jr., Sequestration of Sr (II) by calcium oxalate—a batch uptake study and EXAFS analysis of model compounds and reaction products, Geochim. Et. Cosmochim. Acta 72 (2008) 5055–5069.
[21] A. Mazen, O. El Maghraby, Accumulation of cadmium, lead and strontium, and a role of calcium oxalate in water hyacinth tolerance, Biol. Plant. 40 (1997) 411–417.
[22] Q.T.N. Le, E.L. Vivas, K. Cho, Oxalated blast-furnace slag for the removal of Cobalt (II) ions from aqueous solutions, J. Ind. Eng. Chem. 95 (2021) 57–65, https://doi.org/10.1016/j.jiec.2020.12.003.
[23] X.-Y. Sun, C.-Y. Zhang, P. Bhadja, J.-M. Ouyang, Preparation, properties, formation mechanisms, and cytotoxicity of calcium oxalate monohydrate with various morphologies, CrystEngComm 20 (2018) 75–87.
[24] Y. Kuwahara, S. Tamagawa, T. Fujitani, H.J.Jo.M.C.A. Yamashita, A novel conversion process for waste slag: synthesis of calcium silicate hydrate from blast furnace slag and its application as a versatile adsorbent for water purification, 1 (2013) 7199–7210.
[25] P. Yu, R.J. Kirkpatrick, B. Poe, P.F. McMillan, X.J.JotA.C.S. Cong, Structure of calcium silicate hydrate (C-S-H): Near-, Mid-, and Far-infrared spectroscopy, 82 (1999) 742–748.
[26] B. Xu, Y. Yi, Soft clay stabilization using ladle slag-ground granulated blastfurnace slag blend, Appl. Clay Sci. 178 (2019), 105136.
[27] G. Geng, R.J. Myers, J. Li, R. Maboudian, C. Carraro, D.A. Shapiro, P.J.J.Sr Monteiro, Aluminum-induced dreierketten chain cross-links increase the mechanical properties of nanocrystalline calcium aluminosilicate hydrate, 7 (2017) 1–10.
[28] K.A. Cychosz, R. Guillet-Nicolas, J. García-Martínez, M. Thommes, Recent advances in the textural characterization of hierarchically structured nanoporous materials, Chem. Soc. Rev. 46 (2017) 389–414.
[29] J. Li, Q. Duan, Z. Wu, X. Li, K. Chen, G. Song, A. Alsaedi, T. Hayat, C. Chen, Few-layered metal-organic framework nanosheets as a highly selective and efficient scavenger for heavy metal pollution treatment, Chem. Eng. J. 383 (2020), 123189.
[30] J. Zhao, Y.-J. Zhu, J. Wu, J.-Q. Zheng, X.-Y. Zhao, B.-Q. Lu, F. Chen, Chitosan-coated mesoporous microspheres of calcium silicate hydrate: environmentally friendly synthesis and application as a highly efficient adsorbent for heavy metal ions, J. Colloid Interface Sci. 418 (2014) 208–215.
[31] P. Wang, T. Shen, X. Li, Y. Tang, Y. Li, Magnetic mesoporous calcium carbonate-based nanocomposites for the removal of toxic Pb (II) and Cd (II) ions from water, ACS Appl. Nano Mater. 3 (2020) 1272–1281.
[32] A.E. Gabor, C.M. Davidescu, A. Negrea, M. Ciopec, M. Butnariu, C. Ianasi, C. Muntean, P. Negrea, Lanthanum separation from aqueous solutions using magnesium silicate functionalized with tetrabutylammonium dihydrogen phosphate, J. Chem. Eng. Data 61 (2016) 535–542.
[33] D.D. Do, Adsorption Analysis: Equilibria and Kinetics, Imperial College Press, London, 1998.
[34] M.E. Mahmoud, M.F. Amira, S.M. Seleim, A.K. Mohamed, Amino-decorated magnetic metal-organic framework as a potential novel platform for selective removal of chromium (Vl), cadmium (II) and lead (II), J. Hazard. Mater. 381 (2020), 120979, https://doi.org/10.1016/j.jhazmat.2019.120979.
[35] Y. Peng, H. Huang, Y. Zhang, C. Kang, S. Chen, L. Song, D. Liu, C. Zhong, A versatile MOF-based trap for heavy metal ion capture and dispersion, Nat. Commun. 9 (2018) 1–9.
[36] J. Su, L. Bi, C. Wang, T. Lyu, G. Pan, Enhancement of cadmium removal by oxygen-doped carbon nitride with molybdenum and sulphur hybridization, J. Colloid Interface Sci. 556 (2019) 606–615.
[37] L. Lihua, T. Li, G. Yang, Y. Wang, A. Tang, Y. Ling, Synthesis of thiol-functionalized mesoporous calcium silicate and its adsorption characteristics for heavy metal ions, J. Environ. Chem. Eng. 5 (2017) 6201–6215.
[38] L. Ma, Q. Wang, S.M. Islam, Y. Liu, S. Ma, M.G. Kanatzidis, Highly selective and efficient removal of heavy metals by layered double hydroxide intercalated with the MoS_4^{2-}ion, J. Am. Chem. Soc. 138 (2016) 2858–2866.
[39] L.J.P. Ahrens, C.o.t. Earth, The significance of the chemical bond for controlling the geochemical distribution of the elements-part 1, 5 (1964) 1–54.
[40] M.B. McBride, Environmental Chemistry of Soils, Oxford University Press, 1994.
[41] D.W. Smith, Ionic hydration enthalpies, J. Chem. Educ. 54 (1977) 540, https://doi.org/10.1021/ed054p540.
[42] H. Xu, D.C. Xu, Y. Wang, Natural indices for the chemical hardness/softness of metal cations and ligands, ACS Omega 2 (2017) 7185–7193, https://doi.org/10.1021/acsomega.7b01039.
[43] J. Qu, X. Tian, Z. Jiang, B. Cao, M.S. Akindolie, Q. Hu, C. Feng, Y. Feng, X. Meng, Y. Zhang, Multi-component adsorption of Pb (II), Cd (II) and Ni (II) onto microwave-functionalized cellulose: kinetics, isotherms, thermodynamics, mechanisms and application for electroplating wastewater purification, J. Hazard. Mater. 387 (2020), 121718.
[44] B. Helena, R. Pardo, M. Vega, E. Barrado, J.M. Fernandez, L. Fernandez, Temporal evolution of groundwater composition in an alluvial aquifer (Pisuerga River,

Spain) by principal component analysis, Water Res. 34 (2000) 807–816, https://doi.org/10.1016/S0043-1354(99)00225-0.

[45] N. Kumar, E. Fosso-Kankeu, S.S. Ray, Achieving controllable MoS_2 nanostructures with increased interlayer spacing for efficient removal of Pb (II) from aquatic systems, ACS Appl. Mater. Interfaces 11 (2019) 19141–19155.

[46] J. Zou, C. Guo, X. Zhou, Y. Sun, Z.J.C. Yang, S.A. Physicochemical, E. Aspects, Combining enamel matrix proteins with mechanical stimuli potentiates human periodontal ligament fibroblasts proliferation and periodontium remodeling, Histol. Histopathol. 33 (2018) 825–833.